Eigen Is All You Need: Efficient Lidar-Inertial Continuous-Time Odometry with Internal Association

Thien-Minh Nguyen, *Member, IEEE*, Xinhang Xu, Tongxing Jin, Yizhuo Yang, Jianping Li, Shenghai Yuan, Lihua Xie, *Fellow, IEEE*

Abstract—In this paper, we propose a continuous-time lidarinertial odometry (CT-LIO) system named SLICT2, which promotes two main insights. One, contrary to conventional wisdom, CT-LIO algorithm can be optimized by linear solvers in only a few iterations, which is more efficient than commonly used nonlinear solvers. Two, CT-LIO benefits more from the correct association than the number of iterations. Based on these ideas, we implement our method with a customized solver where the feature association process is performed immediately after each incremental step, and the solution can converge within a few iterations. Our implementation can achieve realtime performance with a high density of control points while yielding competitive performance in highly dynamical motion scenarios. We demonstrate the advantages of our method by comparing with other existing state-of-the-art CT-LIO methods. For the benefits of the community, the source code is released at https://github.com/brytsknguyen/slict.

I. Introduction

Continuous-time optimization has emerged as a new paradigm for lidar-based odometry and mapping (LOAM) systems in recent years. In general, the key aspect that differentiates continuous-time LOAM (CT-LOAM) from discretetime systems is the use of raw lidar points in the optimization process, and the state estimates are formulated directly at the lidar point's sampling time. On the contrary, in traditional discrete-time systems, only a number of state estimates at discrete time instances are created, and some approximation technique is needed to convert the lidar point to a measurement that matches the state estimate's time (see the comparison in Fig. 1). The formulation of the instantaneous state estimate in continuous-time optimization can be based on piece-wise linear interpolation (PLI) [1], [2] or B-spline polynomials [3], [4], [5], [6]. Indeed, the B-spline formulation offers several advantages over the piece-wise linear model. Specifically, it can model the fast-changing trajectory better, fuse data of irregular sampling time, forgo IMU preintegration, and naturally supports online temporal offset estimation. However, it comes to our attention that the computational efficiency of CT-LOAM is still a bottleneck and has not been addressed adequately. This has motivated us to set out the investigation in this paper to obtain more insights on this issue.

All authors are with the School of Electrical and Electronic Engineering, Nanyang Technological University, Singapore 639798, 50 Nanyang Avenue. This research is supported by the National Research Foundation, Singapore under its Medium Sized Center for Advanced Robotics Technology Innovation. Corresponding author: Thien-Minh Nguyen (email: thienminh.npn@ieee.org).

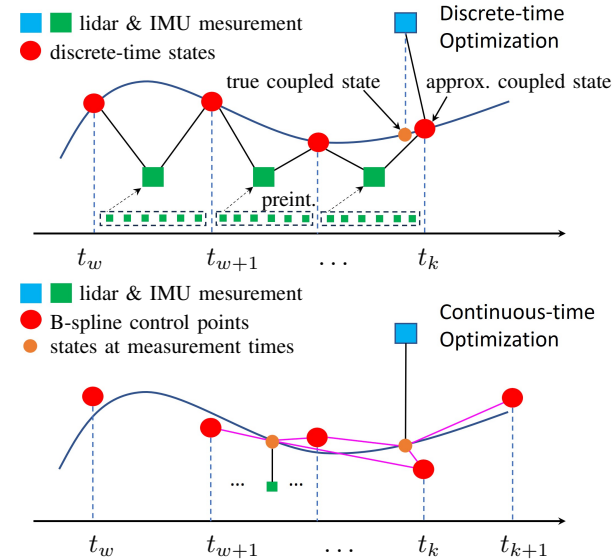


Fig. 1. Comparison between discrete-time (top) and continuous-time (bottom) optimization schemes. In the discrete case, measurements are coupled with distinct state estimates on a sliding window. Often, measurements are not acquired at the state's timestamp, thus some techniques are needed to enforce this strict state-measurement coupling paradigm. For example, the IMU measurements (small green squares) need to be preintegrated to provide a factor that couples two consecutive discrete states (large green squares). On the other hand, for continuous-time optimization, measurements can be coupled directly with the trajectory estimate via the interpolated states. These interpolated states can be understood as time-weighted combination of the control points – the actual decision variable in our optimization problem. In this illustration, we imply a spline order N=3, hence, each interpolated state is coupled with three control points (the pink segments).

For some background, LOAM systems often employ some nonlinear solver (NLS) that optimizes a least-squares cost function by the Gauss-Newton method, of which Ceres-GTSAM-g2o [7], [8], [9] is the dominant trio. Fundamentally, these solvers aim to solve a large least squares problem, in which individual square error terms are constructed and declared locally. The use of NLS offers several advantages. Most importantly, they allow one to tackle the problem in a divide-and-conquer manner, in which user only needs to focus on describing the residual and Jacobian of the individual factors with the locally-coupled states, whereas the arrangement of these residuals and Jacobians at the global scope is automatically managed by the solver. In addition, the NLS can provide extra features such as robust function to suppress outliers, options to exploit the sparseness of the problem, and in-depth diagnosis of the optimization process.

We also note that among the solvers, Ceres is commonly used in tightly-coupled CT-LOAM systems. In our opinion, this is because GTSAM and g2o were originally developed

for visual-odometry problems with elaborate factor graphs. However, these factors are, and should be, fixed for the whole lifespan of the graph, and can be used for both short-term (odometry) and long-term (bundle adjustment) optimization processes. On the other hand, LOAM problems have a much simpler factor graph focusing on a short sliding window, and when the map is updated, the plane / edge coefficients in each factor will also change. Hence the cost function has to be rebuilt each time the map is updated.

SLICT2 is inspired by our previous work SLICT [2], where our primary goal is to upgrade the continuous-time trajectory formulation from PLI to B-spline for the benefits mentioned earlier, while still retaining the competitive performance thanks to the use of multi-resolution incremental mapping and feature association scheme. Following the conventional wisdom, we originally employ the NLS in the B-spline optimization process. However the drawback of non-real-time performance in SLICT still persists. Indeed, the real time issue is not exclusive to SLICT but most CT-LOAM methods. By a thorough investigation, it came to our attention that the NLS incurs significant time overheads when building the least-square problem. Moreover, internal procedures to guarantee monotonic decrease of the cost function also requires extra time, rendering the NLS unappealing. In seeking a remedy for the real time issue, we find that a straightforward approach turns out to yield much better result. Specifically, by forgoing the NLS approach and directly implementing an on-manifold optimization solver based on the Eigen library ¹ (a library for linear algebra operations ubiquitous in robotics research), the CT-LIO problem can converge within a few iterations. In fact, after the first iteration, the state estimate is already good enough for a better association. Therefore, we combine these processes into a solve-associate-solve loop which can converge in 2 or 3 iterations. Effectively, our CT-LIO system acheives both time efficiency (experiments show that it can be up to 8 times faster than using NLS) and competitive accuracy. Moreover, there is no compromise in performance even with a very dense number of control points and lidar factors, which we find to be an issue in other works. In summary, the contribution of SLICT2 can be stated as follows:

- An efficient real-time CT-LIO pipeline with few iterations based on the linear solver of Eigen library and internal feature-to-map association applied between each iteration.
- A detailed local-to-global formulation of the residual and Jacobian of the lidar and IMU factors over the B-spline control points, crucial for the computational efficiency of SLICT2.
- Extensive experiments and analysis to demonstrate the competitive performance of SLICT2 over state-of-theart (SOTA) CT-LIO methods, with an in-depth investigation into the time expenditures of the sub-processes.
- We release our work for the benefits of the community. The remaining of this paper is organized as follows: in

Sec. II, we present the basic notations and the theoretical background of the system. Sec. III provides descriptions of the main steps in the SLICT2 pipeline, and the calculations of the residual and Jacobian of the lidar and inertial factors. In Sec. IV, we perform comparisons of SLICT2 with other SOTA continuous-time lidar odometry methods, and then go deeper into our algorithm to investigate the time cost of each underlying process. Sec. V concludes our work.

II. PRELIMINARIES

A. Notations

For a quantity \mathbf{x} , we use the breve notation $\check{\mathbf{x}}$ to indicate a measurement of \mathbf{x} , and $\hat{\mathbf{x}}$ its estimate. For a matrix \mathbf{x} , \mathbf{x}^{\top} denotes its transpose. For $\mathbf{r} \in \mathbb{R}^n$ and $\mathbf{M} \in \mathbb{R}^{n \times n}$, we denote $\|\mathbf{r}\|_{\mathbf{M}}^2 \triangleq \mathbf{r}^{\top} \mathbf{M} \mathbf{r}$. For a transformation matrix $\mathbf{T} \in \mathrm{SE}(3)$, we also use the expression $\mathbf{T} = (\mathbf{R}, \mathbf{p})$, where $\mathbf{R} \in \mathrm{SO}(3)$ and $\mathbf{p} \in \mathbb{R}^3$ are respectively the rotation and translation components of \mathbf{T} .

We denote the *Lie algebra* group (group of skew-symmetric matrices) as $\mathfrak{so}(3)$, and use $(\cdot)_{\times}$ and $(\cdot)_{\vee}$ to denote the mappings $(\cdot)_{\times} \colon \mathbb{R}^3 \to \mathfrak{so}(3)$ and $(\cdot)_{\vee} \colon \mathfrak{so}(3) \to \mathbb{R}^3$. In addition, the mapping $\operatorname{Exp} \colon \mathbb{R}^3 \to \operatorname{SO}(3)$ and its inverse $\operatorname{Log} \colon \operatorname{SO}(3) \to \mathbb{R}^3$ will also be invoked in subsequent parts. We also use the operator $\boxplus \colon \mathcal{M} \times \mathbb{R}^n \to \mathcal{N}$ to indicate the generalized addition operation on manifolds. We also recall the right Jacobian and the inverse right Jacobian of $\operatorname{SO}(3)$ as J_r and J_r^{-1} defined in [10], [11]. Their closed-form formula is as follows:

$$J_{r}(\phi) = \mathbf{I} - \frac{1 - \cos(\|\phi\|)}{\|\phi\|^{2}} \phi_{\times} + \frac{\|\phi\| - \sin(\|\phi\|)}{\|\phi\|^{3}} (\phi_{\times})^{2},$$

$$J_{r}^{-1}(\phi) = \mathbf{I} + \frac{1}{2} \phi_{\times} + \left(\frac{1}{\|\phi\|^{2}} - \frac{1 + \cos(\|\phi\|)}{2 \|\phi\| \sin(\|\phi\|)}\right) (\phi_{\times})^{2},$$

for $\phi \in \mathbb{R}^3$.

B. B-spline based interpolation

A *B-spline* is a piece-wise polynomial defined by the following parameters: $knot\ length\ \Delta t$, spline $order\ N$ (or alternatively the $degree\ D\triangleq N-1$), and the set of $control\ points\ \{\mathbf{T}_m\}_{m=0}^M,\ \mathbf{T}_m\in \mathrm{SE}(3).$ Each control point \mathbf{T}_m is associated with a knot, denoted as t_m , where $t_m=t_0+m\Delta t$. Given N, a $blending\ matrix\ \mathbf{B}^{(N)}$ and its $cumulative\ form\ \tilde{\mathbf{B}}^{(N)}$ can be calculated as follows:

$$\mathbf{B}^{(N)} = [b_{m,n}] \in \mathbb{R}^{N \times N}; \ m, n \in \{0, \dots N - 1\},$$
 (1)

$$\tilde{\mathbf{B}}^{(N)} = [\tilde{b}_{m,n}]; \ \tilde{b}_{m,n} = \sum_{j=m}^{D} b_{j,n}, \tag{2}$$

$$b_{m,n} = \frac{1}{n!(D-n)!} \sum_{l=m}^{D} (-1)^{l-m} C_N^{l-m} (D-l)^{D-n}.$$
 (3)

note that $C_D^n = \frac{D!}{n!(D-n)!}$ denotes the binomial coefficients. From the control points and the set of knots, for any time $t \in [t_0, t_{M-N+2}]$, which is the sampling time of

¹https://eigen.tuxfamily.org

some measurement, we can interpolate the pose $\mathbf{T}(t) = (\mathbf{R}(t), \mathbf{p}(t))$ at this time by the procedure:

$$s = (t - t_i)/\Delta t, \ t \in [t_i, t_{i+1}), \ t_i \in \{t_m\}_{m=0}^M,$$
 (4)

$$[\lambda_0 \ \lambda_1 \ \dots \ \lambda_{N-1}]^{\top} = \mathbf{B}^{(N)} [1 \ s \ \dots \ s^{N-1}]^{\top}, \quad (5)$$

$$[\tilde{\lambda}_0 \ \tilde{\lambda}_1 \ \dots \ \tilde{\lambda}_{N-1}]^{\top} = \tilde{\mathbf{B}}^{(N)} [1 \ s \ \dots \ s^{N-1}]^{\top},$$
 (6)

$$\mathbf{R}(t) = \mathbf{R}_i \prod_{j=1}^{N-1} \operatorname{Exp}\left(\tilde{\lambda}_j \operatorname{Log}\left(\mathbf{R}_{i+j-1}^{-1} \mathbf{R}_{i+j}\right)\right).$$
 (7)

$$\mathbf{p}(t) = \mathbf{p}_i + \sum_{j=1}^{N-1} \lambda_j \mathbf{p}_{i+j}.$$
 (8)

In other words, given the time t, we first find the knot t_i and the corresponding interval $[t_i, t_{i+1})$ that contains t, then calculate the normalized time s, as conveyed in step (4). Next, we calculate the scaling coefficients λ_i , $\tilde{\lambda}_i$, $i=0,\ldots N-1$ by using the blending matrix and the powers of s in steps (5) and (6). Finally, we calculate the interpolated pose $(\mathbf{R}(t), \mathbf{p}(t))$ at time t by the scaling coefficients and N control points at knots $t_i, \ldots t_{i+N-1}$ in (7) and (8).

Remark 1. Note that for a predefined spline, the above procedure is only applicable for sampling time t not exceeding t_{M-N+2} . Inversely, to represent a trajectory over an interval $[t_{min}, t_{max}]$ by a B-spline with knot length Δt , we set $t_0 = t_{min}$ and the last knot will have the index $M = \lceil (t_{max} - t_{min})/\Delta t \rceil + N - 2$. In Fig. 1, a sliding window with M = 4 and N = 3 is shown. Since N = 3, one control point at time t_{k+1} has to be added for the B-spline to be completely defined on the interval $[t_w, t_k]$, where all of the measurements are being considered. The basalt² library [12] is used to aid in the B-spline formulation in our work.

For convenience in later calculations of residual and Jacobian, we also define the following quantities:

$$[\dot{\tilde{\lambda}}_0 \ \dot{\tilde{\lambda}}_1 \ \dots \ \dot{\tilde{\lambda}}_{N-1}]^{\top} = \tilde{\mathbf{B}}^{(N)} [0 \ 1 \ \dots \ \dot{s}^j \dots \ \dot{s}^{N-2}]^{\top}, \quad (9)$$

$$[\ddot{\lambda}_0 \ \ddot{\lambda}_1 \ \dots \ \ddot{\lambda}_{N-1}]^{\top} = \mathbf{B}^{(N)}[0 \ 0 \ \dots \ \ddot{s}^j \dots \ \ddot{s}^{N-2}]^{\top}, (10)$$

$$\mathbf{d}_{j} = \operatorname{Log}\left(\mathbf{R}_{i+j-1}^{-1}\mathbf{R}_{i+j}\right), \quad \mathbf{A}_{j} = \operatorname{Exp}\left(\tilde{\lambda}_{i}\mathbf{d}_{j}\right),$$
 (11)

$$\mathbf{P}_{j-1} = \mathbf{P}_j \mathbf{A}_j^{\top}, \quad \mathbf{P}_{N-1} = I, \tag{12}$$

$$\boldsymbol{\omega}^{(j)} = \mathbf{A}_{j-1}^{\top} \boldsymbol{\omega}^{(j-1)} + \dot{\tilde{\lambda}}_{j-1} \mathbf{d}_{j-1}, \ \boldsymbol{\omega}^{0} = \boldsymbol{\omega}^{1} = \mathbf{0},$$
 (13)

$$\boldsymbol{\omega}_t = \boldsymbol{\omega}^{(N)}. \tag{14}$$

and note that $\dot{s}^j=\frac{j}{\Delta t}s^{j-1}$ and $\ddot{s}^j=\frac{j(j-1)}{\Delta t^2}s^{j-2}.$

C. Observation models

Most sensing modality can be characterized by an observation model as follows:

$$h(\mathcal{X}, \mathcal{Z}, \mathcal{M}, \eta) = 0, \tag{15}$$

where \mathcal{X} is the state to be estimated, \mathcal{Z} is some measurement from the sensor, \mathcal{M} is the prior information, and η denotes the noise in the measurement or error in modeling.

If we denote $\hat{\mathcal{X}}$ as an estimate of \mathcal{X} , the quantity $h(\hat{\mathcal{X}},\mathcal{Z},\mathcal{M},0)$ can be referred to as the residual. In some cases \mathcal{M} can be absent or considered part of the observation model $h(\cdot)$. Thus, we may write $h(\mathcal{X},\mathcal{Z},\eta)=0$ and $h(\hat{\mathcal{X}},\mathcal{Z},0)$ as the observation model and the residual, respectively.

In the case of CT-LIO, the IMU and lidar observation models can be expressed as follows:

$$(\mathbf{R}_t^{-1}\dot{\mathbf{R}}_t)_{\vee} + \mathbf{b}_{\omega} + \boldsymbol{\eta}_{\omega} - \boldsymbol{\omega}_t = 0, \tag{16}$$

$$\mathbf{R}_t^{-1}(\ddot{\mathbf{p}}_t + \mathbf{g}) + \mathbf{b}_a + \boldsymbol{\eta}_a - \breve{\mathbf{a}}_t = 0 \tag{17}$$

$$\mathbf{n}^{\top} (\mathbf{R}_t^{\mathrm{B}_t} \check{\mathbf{f}} + \mathbf{p}_t) + \mu - \eta_l = 0, \tag{18}$$

where **R** and **p** are the orientation and position states; $\check{\omega}_t$, $\check{\mathbf{a}}_t$, $\check{\mathbf{b}}_t\check{\mathbf{f}}$ are the angular velocity, acceleration, and lidar range measurements at the time instant t; \mathbf{b}_{ω} and \mathbf{b}_a are the IMU biases; η_{ω} , η_a , η_l are the measurement noise; **g** is the gravity constant; and **n**, μ are the plane coefficients of a neighborhood in the map associated with $\check{\mathbf{f}}$.

To simplify the notation, in the subsequent parts we will denote $r_{\mathcal{L}} \triangleq h(\hat{\mathcal{X}}, {}^{\mathbb{B}_t}\mathbf{f}, 0)$ and $r_{\mathcal{I}} \triangleq h(\hat{\mathcal{X}}, (\boldsymbol{\omega}_t.\mathbf{a}_t), 0)$ as the lidar and IMU residuals.

D. The state estimate

The trajectory of the robots represented by a spline starting from the start time t_0 , and extended as new data are acquired. To keep the problem bounded, we only optimize the control points corresponding to the sliding window spanning the latest interval $[t_s,t_e]$. Specifically, the states to be estimated are:

$$\mathcal{X} = (\mathbf{T}_w, \mathbf{T}_{w+1}, \dots \mathbf{T}_{k+N-2}, \mathbf{b}_\omega, \mathbf{b}_a), \qquad (19)$$

where $\mathbf{T}_w, \mathbf{T}_{w+1}, \dots \mathbf{T}_{k+N-2}$ are the control points on the sliding window, with $[t_s, t_e] \subset [t_w, t_{k+N-2}]$, and $\mathbf{b}_{\omega}, \mathbf{b}_a$ are the IMU biases.

Different from discrete-time case where velocity state is often included, in CT-LIO, it is implied in the first order derivative of the position states. Note that one can also include other states such as the local gravity constant, the lidar-IMU offset, and the timestamp offset. However these extra features are beyond the scope of this paper and we believe users can easily modify the basic pipeline of SLICT2 to address these issues should the need arises.

III. METHODOLOGY

A. Main Workflow

Fig. 2 presents the main workflow of SLICT2. The numbering of these blocks conincide with the sections below. The blocks in blue (1, 2.1, 2.2, 4) are inspired by SLICT, which are briefly recapped to provide some background information. The original contributions of SLICT2 are highlighted in red (3.1, 3.2, 3.3), which will be elaborated in details.

1) Synchronization: In the synchronization process, the IMU and lidar data are buffered and organized in so-called bundles. Each bundle consists of a set of raw lidar points $\{^{\mathbb{B}_t}\check{\mathbf{f}},\ldots\}$ and a set of IMU measurements $\{(\check{\boldsymbol{\omega}}_t,\check{\mathbf{a}}_t),\ldots\}$. We also carefully keep track of the timestamps to maintain the time limits of the sliding window.

²https://vision.in.tum.de/research/vslam/basalt

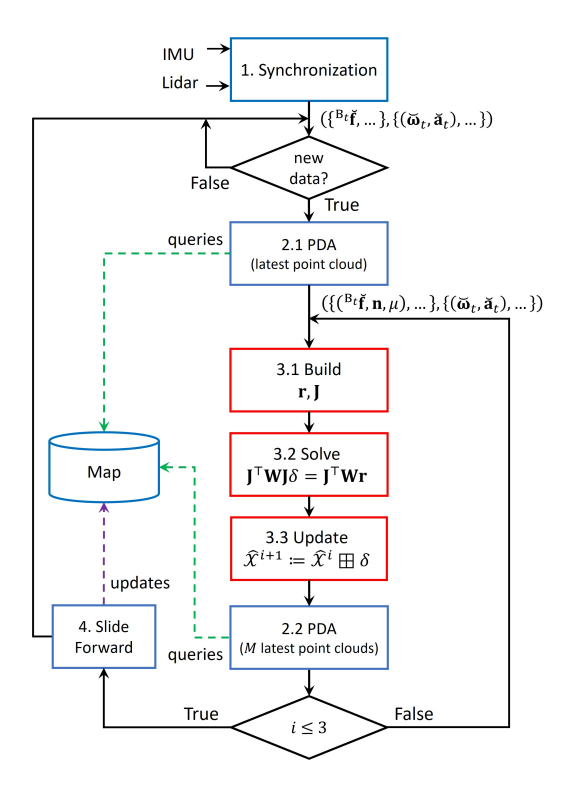


Fig. 2. SLICT2 is a CT-LIO system with a simple yet efficient pipeline. i is the index of the inner loop, starting from 0. We refer to the sequence 3.1 - 3.2 - 3.3 - 2.2 - 3.1 as the *inner loop*, and the *outer loop* refers to the sequence 2.1 - (inner loops) - 2.1. Description of each block is given in Sec. III-A.

2) Propagation-Deskew-Association: Most LIO methods employ the point-to-plane observation model $\mathbf{nf} + \mu = 0$. To obtain the plane coefficients (\mathbf{n}, μ) for each feature $\breve{\mathbf{f}}$, one needs to conduct the following so-called PDA (propagation-deskew-association) procedure:

IMU propagation: When a new bundle of measurements $\left(\left\{ ^{\mathbb{B}_t} \check{\mathbf{f}}, \ldots \right\}, \left\{ (\check{\boldsymbol{\omega}}_t, \check{\mathbf{a}}_t), \ldots \right\} \right)$ is obtained, we will use the IMU measurements $\left\{ (\check{\boldsymbol{\omega}}_t, \check{\mathbf{a}}_t), \ldots \right\}$ to propagate the states and obtain the poses at each IMU sampling time within the step time. This process relies on an initial guess of the state at the first sample. This is why we are motivated to redo propagation after each iteration as we can achieve a better state estimate.

Deskew (motion undistortion): In this step, the *world*-referenced coordinate of ${}^{\mathbb{B}_t}\check{\mathbf{f}}$, denoted as ${}^{\mathbb{W}}\check{\mathbf{f}}$, is obtained by the transform ${}^{\mathbb{W}}\check{\mathbf{f}} = \check{\mathbf{K}}_t{}^{\mathbb{B}_t}\check{\mathbf{f}} + \check{\mathbf{p}}_t$, where $(\check{\mathbf{K}}_t, \check{\mathbf{p}}_t)$ is the pose estimate at the sampling time t of the lidar point $\check{\mathbf{f}}$. This pose estimate can be obtained from sampling the spline (for the old bundles), or by using IMU-propagated pose (for the latest bundle). Again, due to inaccuracy in the propagation step, the deskew process may not be perfect. Hence, a redo can be beneficial after a better state estimate is achieved.

Association: The value $^{\mathbb{N}}\check{\mathbf{f}}$ is used to find a neighbourhood in the map (which can be done by kNN search [13], [14], or proximity to a surfel [15], [2]). Based on the distribution of points in the neighbourhood plane coefficients (\mathbf{n}, μ) can be calculated and associated with $\check{\mathbf{f}}$ for the construction of the point-to-plane factor. Since the two steps need to be done

together, we shall refer to both steps above as the *association* process.

Remark 2. Apparently, all steps in the PDA process rely on some initial estimate of the trajectory, which may not be accurate before thorough optimization. One approach to resolve this issue is to add all possible associable planes [16]. However this approach can be computationally demanding, and wrong associations still have an impact on the overall solution. Therefore, in SLICT2, we opt to simply redoing the association after every update. This is found to be feasible when update step can be done more efficiently with a simple approach, leaving sufficient time for redoing the PDA process after each update.

3) Build, Solve and Update: When all of the measurements \mathcal{Z} on the sliding window have been accounted for, we can begin the so-called Build-Solve-Update (BSU) process. In essence, this process seeks to minimize a cost function f by tuning the state estimate $\hat{\mathcal{X}}$ as follows:

$$f = \sum \left\| r_{\mathcal{L}}(\hat{\mathcal{X}}, {}^{\mathsf{B}_{t}}\check{\mathbf{f}}) \right\|_{\mathbf{W}_{\mathcal{L}}}^{2} + \sum \left\| r_{\mathcal{I}}(\hat{\mathcal{X}}, \check{\boldsymbol{\omega}}_{t}, \check{\mathbf{a}}_{t}) \right\|_{\mathbf{W}_{\mathcal{I}}}^{2} \triangleq \left\| h(\hat{\mathcal{X}}, \mathcal{Z}) \right\|_{\mathbf{W}}^{2}, \quad (20)$$

where $\mathbf{r}_{\mathcal{I}}$ and $\mathbf{r}_{\mathcal{L}}$ are the IMU and lidar resdiuals, $\mathbf{W}_{\mathcal{I}}$, $\mathbf{W}_{\mathcal{L}}$, \mathbf{W} are some weight matrices (often the inverse of covariance), and $h(\hat{\mathcal{X}}, \mathcal{Z})$ is the combined residual vector at the global scope.

To minimize (20), we start with an initial guess $\hat{\mathcal{X}}^0$, then iteratively update $\hat{\mathcal{X}}^i$ by a small perturbation $\delta^* \triangleq \operatorname{argmin}_{\delta} f(\hat{\mathcal{X}}^i \boxplus \delta), i = 1, 2, \ldots$ for multiple steps. To solve the problem $\delta^* \triangleq \operatorname{argmin}_{\delta} f(\hat{\mathcal{X}}^i \boxplus \delta)$ in each iteration, we apply linearization at $\hat{\mathcal{X}}^i$ as follows:

$$f(\hat{\mathcal{X}}^i \boxplus \delta) = \left\| h(\hat{\mathcal{X}}^i \boxplus \delta, \mathcal{Z}) \right\|_{\mathbf{W}}^2 \approx \|\mathbf{r} + \mathbf{J}\delta\|_{\mathbf{W}}^2$$
$$= \delta^{\top} \mathbf{J}^{\top} \mathbf{W} \mathbf{J}\delta + 2\delta^{\top} \mathbf{J}^{\top} \mathbf{W} \mathbf{r} + \mathbf{r}^{\top} \mathbf{W} \mathbf{r}, \quad (21)$$

where $\mathbf{r} = h(\hat{\mathcal{X}}^i, \mathcal{Z})$, and \mathbf{J} is the Jacobian $\frac{\partial h(\hat{\mathcal{X}}^i \boxplus \delta, \mathcal{Z})}{\partial \delta} \Big|_{\substack{\delta \equiv \mathbf{0} \\ \text{The minimum of (21)}}} \Big|_{\substack{\delta \equiv \mathbf{0} \\ \text{The minimum of (21)}}}$.

$$\mathbf{J}^{\top} \mathbf{W} \mathbf{J} \delta = -\mathbf{J}^{\top} \mathbf{W} \mathbf{r}. \tag{22}$$

which is of the form AX = B, and can be solved by a variety of techniques.

Remark 3. As illustrated in Fig. 3, each inner loop consists of one run of the steps 3.1, 3.2, 3.3, 2.2. In NLS-based methods, the steps 3.1, 3.2, 3.3 are handled by a solver, and they can be iterated inside the solver. Empirically, we notice that Ceres would need 7 or 8 iterations for convergence, whereas in SLICT2, we find that we only need 2 or 3 iterations to achieve convergence.

4) Slide Window: At the end of each outer loop, we will judge if the oldest data on the sliding window can be marginalized as a key frame. If the smallest translational or rotational distance of this key frame candidate from K

nearest key frames is larger than a threshold, the candidate can be made into a new key frame. Its point cloud is then inserted to a global map that is used for the PDA process. Our implementation supports both ikdTree [14] and surfel tree [2]. Empirically we find the surfel tree offers better stability and accuracy than ikd-Tree.

B. Residual and Jacobian for B-spline-based factors

In this section we provide the detailed calculation of the residual and the analytical Jacobian of the lidar and inertial factors, which are essential for ensuring real-time performance of the method.

1) Lidar factor: For each lidar feature $^{\text{B}_t}\check{\mathbf{f}}$, based on the observation model (18) and the interpolation rules in Sec. II-B, the residual of the lidar factor can be expressed explicitly as a function of the state estimate (the control points) and the measurements can be put as follows:

$$r_{\mathcal{L}} = \mathbf{n}^{\top} \left[\hat{\mathbf{R}}_{i} \prod_{j=1}^{N-1} \operatorname{Exp} \left(\tilde{\lambda}_{i} \operatorname{Log} \left(\hat{\mathbf{R}}_{i+j-1}^{-1} \hat{\mathbf{R}}_{i+j} \right) \right)^{\operatorname{B}_{t}} \check{\mathbf{f}} \right.$$
$$\left. + \hat{\mathbf{p}}_{i} + \sum_{j=1}^{N-1} \lambda_{i} \left(\hat{\mathbf{p}}_{i+j} - \hat{\mathbf{p}}_{i+j-1} \right) \right] + \mu,$$

where $t \in [t_i, t_{i+1})$. However to handle it more easily, we can write (23) as:

$$r_{\mathcal{L}} = \mathbf{n}^{\top} (\hat{\mathbf{R}}_t^{\mathsf{B}_t} \check{\mathbf{f}} + \hat{\mathbf{p}}_t) + \mu, \tag{23}$$

where $(\hat{\mathbf{R}}_t, \hat{\mathbf{p}}_t)$ is an auxiliary state estimate that is a combination of the decision variables (the control points) that are coupled with $\check{\mathbf{f}}$. Apparently each factor $r_{\mathcal{L}}$ is coupled with N control points, hence its Jacobian over the state estimate $\hat{\mathcal{X}}$ has the form:

$$\frac{\partial r_{\mathcal{L}}}{\partial \hat{\mathcal{X}}} = \left[\cdots \quad \frac{\partial r_{\mathcal{L}}}{\partial \hat{\mathbf{R}}_{i+j}} \quad \frac{\partial r_{\mathcal{L}}}{\partial \hat{\mathbf{p}}_{i+j}} \quad \cdots \right], \tag{24}$$

for $i \in [w, k+N-2]$ such that $[t_i, t_i+1) \ni t, t_i \in \{t_s, \dots t_{k+N-2}\}, j \in \{0, N-1\}$. An illustration of this Jacobian is provided in Fig. 3. To calculate the Jacobian of $r_{\mathcal{L}}$ over $\hat{\mathbf{R}}_{i+j}$ and $\hat{\mathbf{p}}_{i+j}, j \in \{0, 1, \dots, N-1\}$, we apply the chain rule as follows:

$$\frac{\partial r_{\mathcal{L}}}{\partial \hat{\mathbf{R}}_{i+j}} = \frac{\partial r_{\mathcal{L}}}{\partial \hat{\mathbf{R}}_{t}} \frac{\partial \hat{\mathbf{R}}_{t}}{\partial \hat{\mathbf{R}}_{i+j}}, \quad \frac{\partial r_{\mathcal{L}}}{\partial \hat{\mathbf{p}}_{i+j}} = \frac{\partial r_{\mathcal{L}}}{\partial \hat{\mathbf{p}}_{t}} \frac{\partial \hat{\mathbf{p}}_{t}}{\partial \hat{\mathbf{p}}_{i+j}}.$$

Then the task now is to calculate the Jacobians $\frac{\partial r_{\mathcal{L}}}{\partial \hat{\mathbf{R}}_t}$, $\frac{\partial r_{\mathcal{L}}}{\partial \hat{\mathbf{p}}_t}$,

 $\frac{\partial \hat{\mathbf{R}}_t}{\partial \hat{\mathbf{R}}_m}$, and $\frac{\partial \hat{\mathbf{p}}_t}{\partial \hat{\mathbf{p}}_m}$. The first two can be easily calculated as:

$$\frac{\partial r_{\mathcal{L}}}{\partial \hat{\mathbf{R}}_{t}} = \mathbf{n}^{\top} \hat{\mathbf{R}}_{t}^{\mathsf{B}_{t}} \check{\mathbf{f}}_{\times}, \qquad \frac{\partial r_{\mathcal{L}}}{\partial \hat{\mathbf{p}}_{t}} = \mathbf{n}^{\top}, \tag{25}$$

whereas $\frac{\partial \hat{\mathbf{R}}_t}{\partial \hat{\mathbf{R}}_m}$ and $\frac{\partial \hat{\mathbf{p}}_t}{\partial \hat{\mathbf{p}}_m}$ can be found by:

$$\frac{\partial \mathbf{R}_{t}}{\partial \mathbf{R}_{i+j}} = \tilde{\lambda}_{j} \mathbf{P}_{j} J_{r} (\tilde{\lambda}_{j} \mathbf{d}_{j}) J_{r}^{-1} (\mathbf{d}_{j})
- \tilde{\lambda}_{j+1} \mathbf{P}_{j+1} J_{r} (\tilde{\lambda}_{j+1} \mathbf{d}_{j+1}) J_{r}^{-1} (-\mathbf{d}_{j+1}), \quad (26)$$

$$\frac{\partial \mathbf{p}_t}{\partial \mathbf{p}_{i+j}} = \lambda_j I. \tag{27}$$

Equations (26) and (27) are revised from the findings of Sommer *et al* [12] in a more concise and self-contained formula. Note that for the boundary case of j=0, we maintain that (26) can still be applied by defining $\mathbf{A}_0 = \mathbf{R}_i$ and $\mathbf{d}_0 = \operatorname{Log}(\mathbf{R}_i)$; whereas when j=N-1, we define $\tilde{\lambda}_N=0$ and thus one can zero out the second term in (26).

2) *IMU factor:* The residual of IMU factors is defined as:

 $r_{\mathcal{I}} = \begin{bmatrix} r_{\omega} \\ r_{a} \\ r_{b_{\omega}} \end{bmatrix} = \begin{bmatrix} \hat{\boldsymbol{\omega}}_{t} + \hat{\mathbf{b}}_{\omega} - \boldsymbol{\omega}_{t} \\ \hat{\mathbf{a}}_{t} + \hat{\mathbf{b}}_{a} - \boldsymbol{a}_{t} \\ \hat{\mathbf{b}}_{\omega} - \bar{\mathbf{b}}_{\omega} \end{bmatrix} \in \mathbb{R}^{12}, \tag{28}$

where $\hat{\omega}_t$ and $\hat{\mathbf{a}}_t$ are the predicted angular velocity and bodyreferenced acceleration, $\bar{\mathbf{b}}_{\omega}$ and $\bar{\mathbf{b}}_a$ are some prior values of the biases, which are the same as the estimates $\hat{\mathbf{b}}_{\omega}$ and $\hat{\mathbf{b}}_a$ at the end of the previous outer loop. Note that $\hat{\omega}_t$ can be calculated by the formulas (14) and (13), and $\hat{\mathbf{a}}_t$ from (10) and (8).

We see that $r_{\mathcal{I}}$ is coupled with N control points and the two bias states. Thus its Jacobian over the state estimate of (19) will have the following form:

$$\frac{\partial r_{\mathcal{I}}}{\partial \hat{\mathcal{X}}} = \begin{bmatrix}
\dots & \frac{\partial r_{\omega}}{\partial \hat{\mathbf{R}}_{i+j}} & 0 & \dots & I & 0 \\
\dots & \frac{\partial r_{a}}{\partial \hat{\mathbf{R}}_{i+j}} & \frac{\partial r_{a}}{\partial \hat{\mathbf{p}}_{i+j}} & \dots & 0 & I \\
\dots & 0 & 0 & \dots & I & 0 \\
\dots & 0 & 0 & \dots & 0 & I
\end{bmatrix}, (29)$$

Fig. 3 provides an illustration of the structure of this Jacobian. Now, we only need to compute the following Jacobians to complete $\frac{\partial r_{\mathcal{I}}}{\partial \hat{\mathcal{X}}}$:

$$\frac{\partial r_{\omega}}{\partial \hat{\mathbf{R}}_{i+j}} = \frac{\partial \hat{\omega}_t}{\partial \hat{\mathbf{R}}_{i+j}}, \ \frac{\partial r_a}{\partial \hat{\mathbf{R}}_{i+j}} = \frac{\partial \hat{\mathbf{a}}_t}{\partial \hat{\mathbf{R}}_{i+j}}, \ \frac{\partial r_a}{\partial \hat{\mathbf{p}}_{i+j}} = \frac{\partial \hat{\mathbf{a}}_t}{\partial \hat{\mathbf{p}}_{i+j}}.$$

Indeed, the later two can be easily calculated as follows:

$$\frac{\partial \hat{\mathbf{a}}_{t}}{\partial \hat{\mathbf{R}}_{i+j}} = (\hat{\mathbf{a}}_{t})_{\times} \frac{\partial \hat{\mathbf{R}}_{t}}{\partial \hat{\mathbf{R}}_{i+j}}, \quad \frac{\partial \hat{\mathbf{a}}_{t}}{\partial \hat{\mathbf{p}}_{i+j}} = \hat{\mathbf{R}}_{t}^{-1} \ddot{\lambda}_{j}, \quad (30)$$

where $\frac{\partial \hat{\mathbf{R}}_t}{\partial \hat{\mathbf{R}}_{i+j}}$ follows (26), and $\ddot{\lambda}_j$ follows (10).

Finally, for the Jacobian $\frac{\partial \hat{\omega}_t}{\partial \hat{\mathbf{R}}_{i+j}}$, it can be calculated via the following recursive equation:

$$\frac{\partial \boldsymbol{\omega}^{(j)}}{\partial \mathbf{d}_{i}} = \mathbf{P}_{j} \left(\tilde{\lambda}_{j} \mathbf{A}_{j}^{\top} \boldsymbol{\omega}_{\times}^{(j)} J_{r}(-\tilde{\lambda}_{j} \mathbf{d}_{j}) + \dot{\tilde{\lambda}}_{j} I \right). \tag{31}$$

$$\frac{\partial \boldsymbol{\omega}_t}{\partial \mathbf{R}_{i+j}} = \frac{\partial \boldsymbol{\omega}^{(j)}}{\partial \mathbf{d}_j} J_r^{-1}(\mathbf{d}_j) - \frac{\partial \boldsymbol{\omega}^{(j+1)}}{\partial \mathbf{d}_{j+1}} J_r^{-1}(-\mathbf{d}_{j+1}), \quad (32)$$

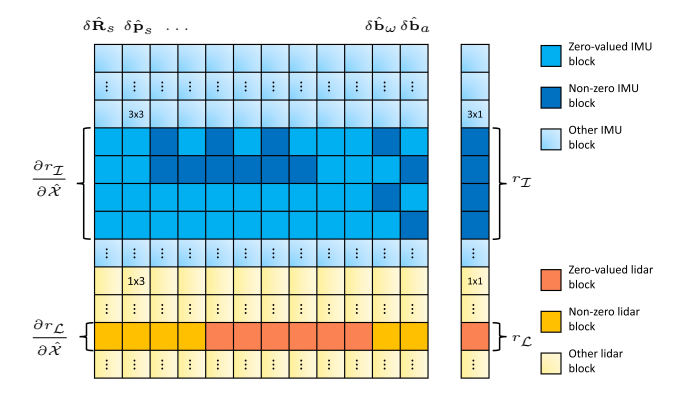


Fig. 3. The structure of the Jacobian (left) and residual (right). The coupling of state estimates with IMU and lidar measurements in this illustration reflect the graph at Fig. 1. Note that the block size represented by each cell is different for IMU and lidar factor. More detailed descriptions are given in Sec. III-B and Sec. III-C.

In (32), for the boundary case
$$j=0$$
 and $j=N-1$, notice that $\frac{\partial \boldsymbol{\omega}^{(0)}}{\partial \mathbf{d}_0} = \frac{\partial \boldsymbol{\omega}^{(N)}}{\partial \mathbf{d}_N} = \mathbf{0}$.

C. Parallelization

The calculation of residual and Jacobian in the previous section is just the first step. To form the equation (22), we still need to map these local computations to the global residual and Jacobian matrices. Apparently this is one of the convenience offered by NLS. However, this can be done more efficiently in a parallelization scheme. First, from the number of IMU and lidar factors, as well as the number of state estimates, we can deduce the appropriate dimensions to allocate the **r** and **J** matrices. Then, we create concurrent threads to calculate and assign values to the sub-blocks of **r** and **J** by the appropriate indices.

An example is used to illustrate this process in reference to Fig. 3. Let us denote $K_{\mathcal{I}}$ and $K_{\mathcal{L}}$ as the number of IMU and lidar factors, S=k-w+1+N-2 as the number of control points (as illustrated in Fig. 1), and X=6S+6 the dimension of all state estimates (consisting of S control points and 2 bias vectors). We can then index the entries in \mathbf{J} and \mathbf{r} as $\mathbf{J}=[J_{m,n}]$ and $\mathbf{r}=[r_m]$, where $m\in\{0,\ldots K_{\mathcal{I}}+K_{\mathcal{L}}-1\}$ and $n\in\{0,\ldots X-1\}$. In our case the residual and Jacobian of IMU factors are stacked above the lidar factors.

Now, for a lidar factor with index $a \in \{0, \dots, K_{\mathcal{L}} - 1\}$, from (23) and (29), we can find that its residual is the single entry $r_{12.K_{\mathcal{I}}+a}$ in the vector \mathbf{r} , while the non-zero entries of its Jacobian reside at $J_{12.K_{\mathcal{I}}+a,n}$, $n \in \{6i, \dots 6i+6N-1\}$, where i is the index of the knot whose interval $[t_i, t_{i+1})$ contains t, the sampling time of the lidar measurement.

Similarly, for an IMU factor with index $b \in \{0, \dots, K_{\mathcal{I}} - 1\}$, its residual includes the entries r_{12b+m} , $m \in \{0, \dots 12\}$, whereas its non-zero Jacobian spreads across the entries $J_{12b+m,n}$, where $(m,n) \in \{0, \dots 6\} \times \{6i, \dots 6i+6N-1\} \cup \{0,12\} \times \{6S, \dots 6S+6-1\}$.

The above analysis is essential to calculating the Jacobian and residuals of thousands of factors in a few miliseconds. The time efficiency of this process is reported in Sec. IV-B.

TABLE I APE of LO and LIO methods on the NTU dataset.

Sequence	FLIO	CLIC	CTICP	SLICT	SLICT2
eee_01	0.069	0.056	6.503	0.024	0.025
eee_02	0.069	0.056	X	0.019	0.023
eee_03	0.111	0.062	X	0.028	0.024
nya_01	0.053	0.069	0.459	0.022	0.021
nya_02	0.090	0.075	0.618	<u>0.026</u>	0.023
nya_03	0.108	0.079	0.129	<u>0.030</u>	0.021
rtp_01	0.125	0.263	9.675	0.056	<u>0.059</u>
rtp_02	0.131	0.150	8.907	0.062	0.056
rtp_03	0.137	0.077	9.894	0.070	0.064
sbs_01	0.086	0.071	X	0.025	0.025
sbs_02	0.078	0.073	3.872	0.033	0.032
sbs_03	0.076	0.066	7.104	0.025	0.028
spms_01	0.210	0.173	20.253	0.057	<u>0.060</u>
spms_02	0.336	X	43.040	0.200	0.198
spms_03	0.174	0.266	23.289	0.062	0.053
tnp_01	0.090	0.221	1.467	0.033	<u>0.041</u>
tnp_02	<u>0.110</u>	0.779	X	X	0.070
tnp_03	0.089	0.382	1.051	0.053	0.042

*All values are in meter. The best APEs among the methods are in **bold**, the second best are <u>underlined</u>. 'x' demotes a divergent experiment. FLIO is short for FAST-LIO2 SLICT2-2R refers to the number of point clouds that undergo reassociations in the inner loop.

IV. EXPERIMENT

A. Accuracy test

In this first part we will compare SLICT2 with other state of the art LIO methods in popular public datasets.

On the methods, the following are selected: FAST-LIO2 [17], CT-ICP[1], SLICT[2], and CLIC[18]. FAST-LIO2 is a seminal discrete-time based LIO method that pioneered the iterated Extended Kalman Filter (iEKF) in LIO. It has also inspired many other works [19], [20], [21], [22] in recent years. For continuous-time, CT-ICP is one of the first publicly released CT-LO methods that use PLI. Similarly, SLICT uses a PLI formulation, but at the sub-interval level of the lidar scan. Finally, CLIC is an improved version of CLINS [4], a LIO method that uses NLS-based B-spline continuous-time formulation.

On the datasets, we select NTU VIRAL [23] as the first benchmark, in which we use the horizontal 16-channel lidar mounted on an aerial vehicle, the high accuracy high frequency IMU, and a centimeter ground truth captured by a laser tracker. Since NTU VIRAL sequences have relatively low speed, we select the high velocity sequences in the Multi-Campus Dataset (MCD) [24] as the next benchmark. Moreover, for the MCD benchmark we also experiment with the non-repetitive lidar (livox), which has gained significant popularity in recent years due to low cost and high accuracy, but also poses a challenge with the narrower field of view.

In all experiments with SLICT2, we set knot length to 0.01s, the spline order is 4, the window size 3, the number of internal iterations 3, the re-associated clouds 2, and the maximum number of lidar factors is capped at 8000. All

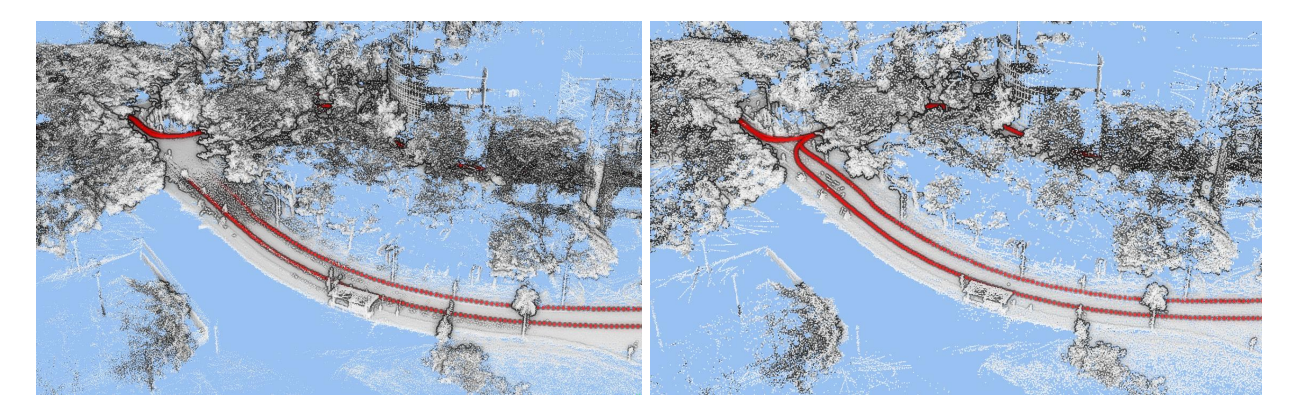


Fig. 4. The map and trajectory (red) of FAST-LIO (left) and SLICT2 (right) in xxx_day_01 sequence. We can see that FAST-LIO has a slight drift in the vertical direction, leading to its larger APE in this sequence.

 $\begin{tabular}{ll} TABLE & II \\ APE & of LO & and LIO & methods & on MCD & dataset. \\ \end{tabular}$

Sequence	FLIO	CLIC	CTICP	SLICT	SLICT2-2R
xxx_day_01	0.901	25.194	X	0.570	0.498
xxx_day_02	0.185	0.503	0.807	0.188	0.169
xxx_day_10	1.975	22.775	64.911	0.842	0.745
xxx_night_04	0.902	4.154	69.024	0.382	0.344
xxx_night_08	1.002	22.275	X	0.651	<u>0.817</u>
xxx_night_13	1.288	21.299	X	2.773	0.631

^{*}All values are in meter. The best APEs among the methods are in **bold**, the second best are <u>underlined</u>. 'x' demotes a divergent experiment.

experiments are carried out on a PC with intel core i9 CPU with 32 threads. Each method is run for 5 times and the best APE (Absolute Position Error) metric reported by the evo package [25] for each sequence is recorded in Tab. I and Tab. II.

For the NTU VIRAL benchmark, we can see that SLICT2 has the best performance by the number of sequences with lowest APE, followed closely by SLICT. FAST-LIO2 and CLIC have somewhat similar performance, while CT-ICP has the lowest performance. The close performance between SLICT and SLICT2 is expected. This is because SLICT2 shares similar frontend with SLICT, and the sequences are at relatively low speed, therefore the advantages of B-spline trajectory representation in SLICT2 is not yet evident over the PLI approach of SLICT. However we can see that SLICT2 does not diverge where SLICT does, which is due to the internal association measure which helps the method converge faster and more accurately in the challenging environment (Fig. 5). We also note that SLICT cannot run in real time even when only a 16-channel lidar is used.

For the MCD benchmark, we have a more definitive result where SLICT2 has the smallest APE in the most sequences. At the second place is SLICT, followed by FLIO. Fig. 4 shows the map and trajectory output of FAST-LIO and SLICT2 in one sequence. This demonstrates the benefit of the B-spline continuous-time formulation with dense number of control points, which can better capture the dynamics of high speed sequence and UAV motion. On the contrary, CT-

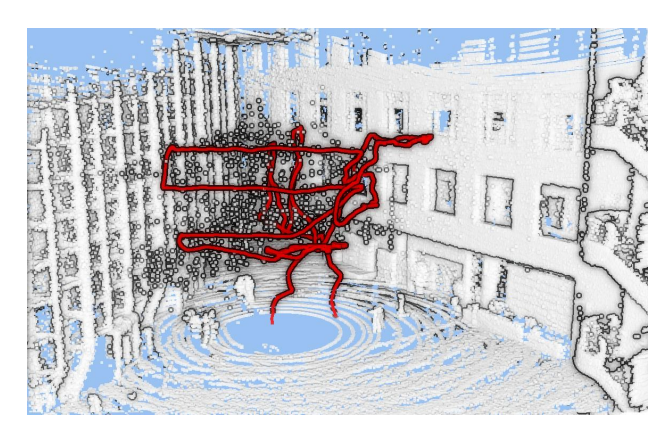


Fig. 5. The environment in the tnp_02 sequence in NTU VIRAL dataset with significant noise from sun glare and glass wall. Also when the UAV is flying high (the trajectory of UAV is in red), there are few features that can constrain the vertical drift. This leads to the divergence of SLICT.

ICP, being a lidar-only method that uses PLI, struggles with the high speed sequences and can easily diverge in some long sequences. Finally, CLIC is slightly better than CT-ICP, however its performance is still not as good as FAST-LIO. It should also be noted that despite its relatively good performance, SLICT cannot run in real time even with the sparse livox point cloud. In addition, CT-ICP and CLIC cannot run in real time with such high number of lidar factors set for SLICT2, and CLIC frequently crashes when we try to set a dense number of control points like SLICT2.

B. Processing time

To study the efficiency of SLICT2, we carefully added multiple timers in the program to record the processing time for each step and sub-step in the xxx_day_01 sequence.

In reference to Fig. 6, we define $t_{\rm outer_loop}$ as the processing time of one outer loop (Fig 2). Next, $t_{\rm pda}$ is defined as the total time for the three PDA iterations in the inner loops and one in the outer loop (step 2.2 and 2.1 in Fig. 2). Similarly, $t_{\rm bsu}$ is the total time of three iterations of the BSU process in the inner loops. Finally, the $t_{\rm other}$ refers to other processes such as copying data, feature selection, visualization, making diagnostic reports etc.

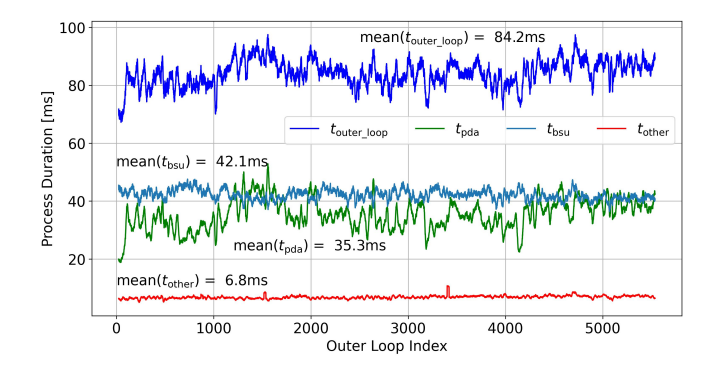


Fig. 6. Processing time of the outer loop, the PDA process, the BSU process, and others. Note that the values have been smoothed out by applying a 20-step sliding window average.

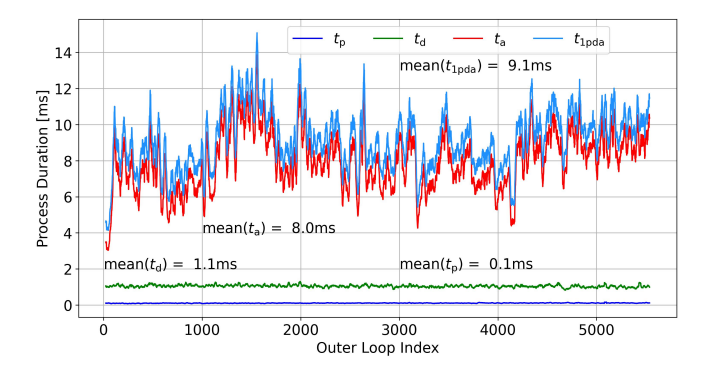


Fig. 7. Processing time of one PDA iteration.

From the plot, $t_{\rm loop}$ maxes at 100ms and the mean value is about 83ms, which confirms that SLICT2 can run in real time. Noteably, $t_{\rm pda}$ varies quite significantly, while $t_{\rm bsu}$ and $t_{\rm other}$ are relatively stable. This is due to the variation in size of the input point clouds, which has direct effect on the processing time for the down-sampling, deskew, and association processes. After the PDA process is completed, the optimization problem has a fixed size of 8000 lidar factors, thus $t_{\rm bsu}$ consumes more or less the same amount of time in every loop.

Fig. 7 shows the processing time of sub-processes of one PDA iteration, where $t_{1\mathrm{pda}}$ refers to the PDA process time of the 1st inner iteration, and t_{prop} , t_{desk} , t_{assoc} the processing time for propagation, deskew, and association respectively. We can see that the majority of processing time is expended on associating the lidar points with the map, while IMU propagation takes less than 1ms, and deskew less than 2ms.

Similarly, we look into one BSU iteration in Fig. 8. Here $t_{1\text{bsu}}$ is the processing time of the BSU sequence in the first inner loop. The processing of step 3.1 is denoted as t_{b} , and the processing time for step 3.2 and 3.3 are lumped together into t_{su} as the update step is quite small compared to others.

It is clearly shown in Fig. 8 that the calculation of residuals and Jacobians of thousands of factors can be completed in a few milliseconds thanks to our parallelization scheme. On the other hand, the majority of time is spent on the solving step. This offers an insight into how the efficiency can be improved: since we only use a solver of the Eigen library for this task, a better solver or library can reduce the time

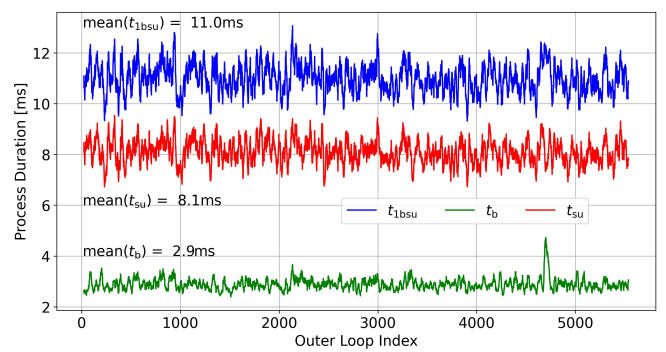


Fig. 8. Processing time of one BSU iteration.

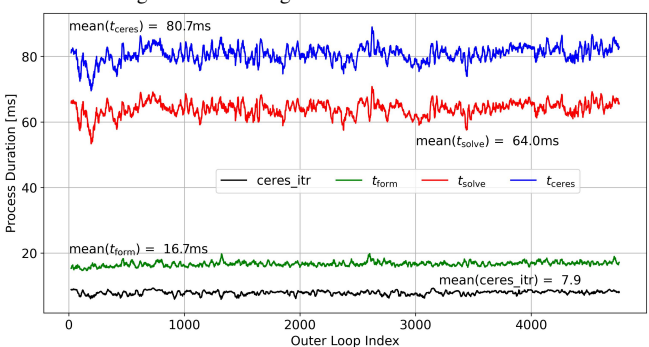


Fig. 9. Processing time of one BSU iteration by using Ceres.

spent on this process.

Finally, to highlight the efficiency of the SLICT2 solver, we replace steps 3.1, 3.2 and 3.3 in our pipeline with a Ceresbased procedure, and record the time costs in Fig. 9. In this plot, $t_{\rm ceres}$ refers to the processing time to build the cost function and solve it with Ceres before moving to step 2.2, $t_{\rm form}$ refers to the time needed to formulate a Ceres problem with 8000 lidar factors (plus a few hundred IMU factors), and $t_{\rm solve}$ is the time needed to optimize the cost function. Here, $t_{\rm solve}$ should be equivalent to $t_{\rm 1bsu}$ in Fig. 8. We also report the number of internal iterations that Ceres takes before reaching the optimal solution, this is referred to as ceres_iter.

First, we notice that $t_{\rm form}$ alone is already longer than the whole BSU process when using SLICT2 solver. This is an overhead that is common for using NLS, not unique to Ceres. We also notice that the average time for Ceres to reach the optimal solution is 64ms, for about 7.9 iterations on average. If we divide 64ms by 7.9, we obtain the average time for an iteration of 8.1ms, which is close to the amount of time that SLICT2 needs for calculating the residual, Jacobian, and solving (22). However, this is only one iteration, and Ceres needs up to 8 iterations to converge due to its internal checks to ensure monotonic decrease in each iteration. This again shows that the NLS-based approach is not as efficient as the method implemented in SLICT2.

C. Ablation study

As shown in Fig. 7, the association process takes the majority of time in the 2.2 step. To justify the iteration of this process in the inner loop, we need to show that it does

 $\label{thm:table} \mbox{TABLE III}$ APE of SLICT2 with different Re-associated point clouds.

Sequence	SLICT2-0	SLICT2-1	SLICT2-2	SLICT2-3
xxx_day_01	0.790	0.527	0.498	0.708
xxx_day_02	0.262	0.183	0.169	0.164
xxx_day_10	1.104	1.181	0.745	0.817
xxx_night_04	0.670	0.466	0.344	0.354
xxx_night_08	2.137	0.706	0.817	0.978
xxx_night_13	2.960	0.771	0.631	0.477

*All values are in meter. For each method, the best result out five runs is reported. The best APEs among the methods are in **bold**, the second best are <u>underlined</u>. 'x' demotes a divergent experiment. SLICT2-M indicates re-associations are applied to the last M point clouds on the sliding window in the inner loop.

improve the APE of the LIO scheme. To this end, we rerun SLICT2 with different number of point clouds undergoing re-association in the inner loop, denoted as M. Since the sliding window has a length of 3, M is changed from 0 to 3 in these experiments.

From Tab. III, we can see that for each sequence, SLICT2-1 is generally improved over SLICT2-0, which is then improved further in SLICT2-2, and the effect does not distinctly improve with 3 re-associations. This shows that the internal association does offer advantageous effects on the accuracy of the CT-LIO system.

V. CONCLUSION

In this paper, we have developed a CT-LIO system using a basic yet efficient optimization approach, named SLICT2. The key innovation in our method is the use of a simple solver which eliminates many computational overheads of conventional NLS, yet still achieves convergent result in only a few iterations. The performance is further enhanced by conducting association between each iteration. We also conduct thorough analysis on the processing time of each step in SLICT2's pipeline to gain insights into its efficiency. The performance of SLICT2 is demonstratively competitive when compared to other SOTA methods, and it can be easily extended to address other issues such as online calibration, temporal offsets, and multi-modal sensor fusion. We believe SLICT2 has made a strong case for more efficient implementation of LIO systems in the future.

REFERENCES

- P. Dellenbach, J.-E. Deschaud, B. Jacquet, and F. Goulette, "Cticp: Real-time elastic lidar odometry with loop closure," in 2022 International Conference on Robotics and Automation (ICRA). IEEE, 2022, pp. 5580–5586.
- [2] T.-M. Nguyen, D. Duberg, P. Jensfelt, S. Yuan, and L. Xie, "Slict: Multi-input multi-scale surfel-based lidar-inertial continuoustime odometry and mapping," *IEEE Robotics and Automation Letters*, vol. 8, no. 4, pp. 2102–2109, 2023.
- [3] J. Quenzel and S. Behnke, "Real-time multi-adaptive-resolution-surfel 6d lidar odometry using continuous-time trajectory optimization," in 2021 IEEE/RSJ International Conference on Intelligent Robots and Systems (IROS). IEEE, 2021, pp. 5499–5506.
- [4] J. Lv, K. Hu, J. Xu, Y. Liu, X. Ma, and X. Zuo, "Clins: Continuous-time trajectory estimation for lidar-inertial system," in 2021 IEEE/RSJ International Conference on Intelligent Robots and Systems (IROS). IEEE, 2021, pp. 6657–6663.

- [5] B. He, W. Dai, Z. Wan, H. Zhang, and Y. Zhang, "Continuous-time lidar-inertial-vehicle odometry method with lateral acceleration constraint," in 2023 IEEE International Conference on Robotics and Automation (ICRA). IEEE, 2023, pp. 3997–4003.
- [6] X. Zheng and J. Zhu, "Traj-lo: In defense of lidar-only odometry using an effective continuous-time trajectory," *IEEE Robotics and Automation Letters*, 2024.
- [7] S. Agarwal and K. Mierle, "Ceres solver: Tutorial & reference." [Online]. Available: http://ceres-solver.org/
- [8] F. Dellaert, R. Roberts, V. Agrawal, A. Cunningham, C. Beall, D.-N. Ta, F. Jiang, lucacarlone, nikai, J. L. Blanco-Claraco, S. Williams, ydjian, J. Lambert, A. Melim, Z. Lv, A. Krishnan, J. Dong, G. Chen, K. Chande, balderdash devil, DiffDecisionTrees, S. An, mpaluri, E. P. Mendes, M. Bosse, A. Patel, A. Baid, P. Furgale, matthewbroadwaynavenio, and roderick koehle, "borglab/gtsam," May 2022. [Online]. Available: https://doi.org/10.5281/zenodo.5794541
- [9] G. Grisetti, R. Kümmerle, H. Strasdat, and K. Konolige, "g2o: A general framework for (hyper) graph optimization," in *Proceedings* of the IEEE International Conference on Robotics and Automation (ICRA), 2011, pp. 9–13.
- [10] J. Sola, J. Deray, and D. Atchuthan, "A micro lie theory for state estimation in robotics," arXiv preprint arXiv:1812.01537, 2018.
- [11] T.-M. Nguyen, M. Cao, S. Yuan, Y. Lyu, T. H. Nguyen, and L. Xie, "Viral-fusion: A visual-inertial-ranging-lidar sensor fusion approach," *IEEE Transactions on Robotics*, vol. 38, no. 2, pp. 958–977, 2022.
- [12] C. Sommer, V. Usenko, D. Schubert, N. Demmel, and D. Cremers, "Efficient derivative computation for cumulative b-splines on lie groups," in *Proceedings of the IEEE/CVF Conference on Computer Vision and Pattern Recognition*, 2020, pp. 11148–11156.
- [13] T.-M. Nguyen, S. Yuan, M. Cao, Y. Lyu, T. H. Nguyen, and L. Xie, "Miliom: Tightly coupled multi-input lidar-inertia odometry and mapping," *IEEE Robotics and Automation Letters*, vol. 6, no. 3, pp. 5573– 5580, May 2021.
- [14] W. Xu and F. Zhang, "Fast-lio: A fast, robust lidar-inertial odometry package by tightly-coupled iterated kalman filter," *IEEE Robotics and Automation Letters*, vol. 6, no. 2, pp. 3317–3324, 2021.
- [15] C. Park, P. Moghadam, S. Kim, A. Elfes, C. Fookes, and S. Sridharan, "Elastic lidar fusion: Dense map-centric continuous-time slam," in 2018 IEEE International Conference on Robotics and Automation (ICRA). IEEE, 2018, pp. 1206–1213.
- [16] K. Koide, M. Yokozuka, S. Oishi, and A. Banno, "Voxelized gicp for fast and accurate 3d point cloud registration," in 2021 IEEE International Conference on Robotics and Automation (ICRA). IEEE, 2021, pp. 11054–11059.
- [17] W. Xu, Y. Cai, D. He, J. Lin, and F. Zhang, "Fast-lio2: Fast direct lidar-inertial odometry," *IEEE Transactions on Robotics*, vol. 38, no. 4, pp. 2053 2073, 2022.
- [18] J. Lv, X. Lang, J. Xu, M. Wang, Y. Liu, and X. Zuo, "Continuoustime fixed-lag smoothing for lidar-inertial-camera slam," *IEEE/ASME Transactions on Mechatronics*, 2023.
- [19] J. Lin and F. Zhang, "R3live: A robust, real-time, rgb-colored, lidar-inertial-visual tightly-coupled state estimation and mapping package," in 2022 International Conference on Robotics and Automation (ICRA). IEEE, 2022, pp. 10672–10678.
- [20] C. Bai, T. Xiao, Y. Chen, H. Wang, F. Zhang, and X. Gao, "Faster-lio: Lightweight tightly coupled lidar-inertial odometry using parallel sparse incremental voxels," *IEEE Robotics and Automation Letters*, vol. 7, no. 2, pp. 4861–4868, 2022.
- [21] C. Zheng, Q. Zhu, W. Xu, X. Liu, Q. Guo, and F. Zhang, "Fast-livo: Fast and tightly-coupled sparse-direct lidar-inertial-visual odometry," in 2022 IEEE/RSJ International Conference on Intelligent Robots and Systems (IROS). IEEE, 2022, pp. 4003–4009.
- [22] Z. Chen, Y. Xu, S. Yuan, and L. Xie, "ig-lio: An incremental gicp-based tightly-coupled lidar-inertial odometry," *IEEE Robotics and Automation Letters*, 2024.
- [23] T.-M. Nguyen, S. Yuan, M. Cao, Y. Lyu, T. H. Nguyen, and L. Xie, "Ntu viral: A visual-inertial-ranging-lidar dataset, from an aerial vehicle viewpoint," *The International Journal of Robotics Research*, vol. 41, no. 3, pp. 270–280, 2022.
- [24] T.-M. Nguyen, S. Yuan, T. H. Nguyen, P. Yin, H. Cao, L. Xie, M. Wozniak, P. Jensfelt, M. Thiel, J. Ziegenbein, and N. Blunder, "Mcd: Diverse large-scale multi-campus dataset for robot perception," in *Proceedings of the IEEE/CVF Conference* on Computer Vision and Pattern Recognition, Jun. 2024. [Online]. Available: https://mcdviral.github.io/
- [25] M. Grupp, "evo: Python package for the evaluation of odometry and slam." https://github.com/MichaelGrupp/evo, 2017.